

Calculated fission-fragment mass yields and average total kinetic energies of heavy and superheavy nuclei

Martin Albertsson^{1,a}, B. Gillis Carlsson¹, Thomas Døssing², Peter Möller¹, Jørgen Randrup³, and Sven Åberg¹

¹ Mathematical Physics, Lund University, S-221 00 Lund, Sweden

² Niels Bohr Institute, University of Copenhagen, DK-2100 Copenhagen Ø, Denmark

³ Nuclear Science Division, Lawrence Berkeley National Laboratory, Berkeley, California 94720, USA

Received: date / Revised version: date

Abstract. Fission-fragment mass and total-kinetic-energy (TKE) distributions following fission of even-even nuclides in the region $74 \leq Z \leq 126$ and $92 \leq N \leq 230$, comprising 896 nuclides have been calculated using the Brownian shape-motion method. The emphasis is the region of superheavy nuclei. To show compatibility with earlier results the calculations are extended to include earlier studied regions. An island of asymmetric fission is obtained in the superheavy region, $106 \leq Z \leq 114$ and $162 \leq N \leq 176$, where the heavy fragment is found to be close to ^{208}Pb and the light fragment adjusts accordingly. Most experimentally observed α -decay chains of superheavy nuclei with $Z > 113$ terminate by spontaneous fission in our predicted region of asymmetric fission. In these cases, the pronounced large asymmetry is accompanied by a low TKE value compatible with measurements.

PACS. 24.75.+i – 25.85.Ca – 25.85.-w – 27.80.+w – 27.90.+b

1 Introduction

The seven new elements in the range $107 \leq Z \leq 113$ were all identified through α -decay chains ending in previously observed α decays. However, for the still heavier elements created in ^{48}Ca -induced fusion-evaporation reactions it is more involved to establish the specific isotope created since most α -decay chains end in spontaneous fission and not in a previously known α decay. For an overview, see refs. [1,2]. To contribute to the interpretation of these experimental results we calculate fission-fragment mass and kinetic-energy distributions and average total kinetic-energies (TKE) for 896 even-even nuclides in the region $74 \leq Z \leq 126$ and $92 \leq N \leq 230$. We use the Brownian shape-motion (BSM) method [3] which has been extensively compared to experimental data [4] and used in studies of the “new region of asymmetry” in the neutron-deficient Pb region [5,6].

2 Computational details

The first step is to calculate the potential-energy surfaces as functions of five shape parameters. In previous publications [3,4,6,7,8,9] potential-energy surfaces calculated in ref. [10] have been used. The current calculations are also done as specified in ref. [10] but with one difference: In

the Strutinsky shell-correction procedure we use a larger smoothing range

$$\gamma = 1.5 \times \frac{41 \text{ MeV}}{A^{1/3}} B_S, \quad (1)$$

where B_S is the ratio of the surface area of the current shape to that of a spherical shape. This is particularly important for nuclei in the vicinity of fermium (Fm) as discussed in great detail in refs. [11,12].

In the calculation, most of the CPU time is used to calculate the single-particle levels. Once the levels are determined, the time needed to calculate the shell and pairing corrections and macroscopic contributions to the potential energy is almost negligible. Therefore we use the same set of levels to calculate the shell corrections for several neighbouring nuclei, which still leads to satisfactory accuracy. We use levels calculated for four “center” nuclei, namely ^{214}Rn , ^{288}Pu , ^{258}Fm , and ^{270}Hs . This strategy is routinely employed when calculating the potential energy for neighbouring nuclei [3,10,13,14,15,16] and is sufficiently accurate for our overview here. As pointed out in sect. 3.1, we obtain very similar results as ref. [6], for the region where our two studies overlap, even though potentials for somewhat different nuclei are used to calculate the single-particle levels and the corresponding shell corrections.

The critical neck radius, where fragment separation is assumed to occur, is $c_0 = 1.5$ fm. To ensure that the vast majority of the random walks reach this neck radius before reaching the boundary of the employed shape lattice

^a e-mail: martin.albertsson@matfys.lth.se

we have extended the grid with eight additional points in the elongation direction, corresponding to more than one million additional shapes. The largest value of the dimensionless elongation parameter q_2 (defined in eq. (11) in ref. [9]) is extended from roughly 16 to 20.

2.1 Fission-fragment mass distributions

We calculate the fission-fragment mass distributions with the BSM method on the multi-dimensional potential-energy surfaces as specified in refs. [3,4]. The walks are started at the second minimum, when such a minimum exists, otherwise at the ground-state minimum. For the cases where the ground-state shape is spherical, the walk is started at the least deformed symmetric shape included in the grid, corresponding to $\beta_2 \approx 0.12$. We follow the prescription of the earlier study [6] and use the effective level density of ref. [4]. A more refined calculation would employ shape-dependent microscopic level densities as pioneered in ref. [9] but such a huge effort is not computationally feasible yet. Also, we limit the study to even-even nuclei because yields vary insignificantly between neighbouring nuclides except in a few isolated cases. Each distribution is based on 10000 walks. Excitation energies are chosen just sufficiently above the barrier to obtain reasonable computing times. As in ref. [6] the bias potential is 60 MeV. The fission-fragment mass yield $Y(A)$ is defined as the percentage of events resulting in fragment-mass number A . The yield is normalized to 200% because each fission event results in two fragments.

2.2 Total kinetic energies

The total available energy in the fission process is given by the initial excitation energy, E_{exc} , with respect to the ground state of the fissioning nucleus and the Q value,

$$Q^* = E_{\text{exc}} + M(Z, N) - M(Z_L, N_L) - M(Z_H, N_H), \quad (2)$$

where $M(Z, N)$ is the ground-state mass of the parent nucleus, and $M(Z_L, N_L)$ and $M(Z_H, N_H)$ are the ground-state masses of the light and heavy fragments, respectively. The proton and neutron numbers, Z and N , are determined by requiring the same Z/N ratio as for the fissioning nucleus. In the present study only fragments with even Z and N are considered.

The available energy is divided between the total kinetic energy and the total excitation energy of the fragments, *i.e.*,

$$Q^* = E_{\text{TKE}} + E_{\text{TXE}}. \quad (3)$$

The total excitation energy, E_{TXE} , shared between the two fragments, is composed by the two parts, intrinsic excitation energy and deformation energy of the light (L) and heavy (H) fragment,

$$E_{\text{TXE}} = E_{\text{sc}}^* + E_{\text{L}}^{\text{def}} + E_{\text{H}}^{\text{def}}. \quad (4)$$

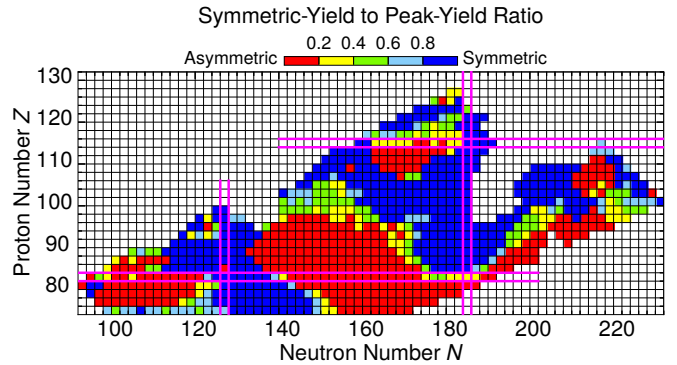


Fig. 1. Calculated symmetric-yield to peak-yield ratios versus N and Z for fissioning nuclides between the proton and neutron drip lines and $74 \leq Z \leq 126$, for even-even nuclides. Nuclides with barriers calculated to be lower than 3 MeV are not included. Pairs of magenta parallel lines indicate magic neutron and proton numbers in the model ($N = 126, 184$ and $Z = 82, 114$).

The intrinsic excitation energy, E_{sc}^* , is the energy difference between the total energy, E_{tot} , and the potential energy at the scission configuration $U(\chi_{\text{sc}})$,

$$E_{\text{sc}}^* = E_{\text{tot}} - U(\chi_{\text{sc}}), \quad (5)$$

where χ denotes the five shape parameters. The deformation energy is released in the fragments after scission when the accelerated fission fragments relax their respective shapes to ground-state deformations. The released energy is thereby added to the internal excitation energy.

The deformation energy of each fragment is calculated as the energy difference between the fragment mass at scission [17] and its ground-state mass,

$$E_i^{\text{def}} = M_i(\varepsilon_i^{\text{sc}}) - M_i(\varepsilon_i^{\text{gs}}), \quad (6)$$

where $i = \text{L}$ or H .

The masses in eqs. (2) and (6), are calculated in the same macroscopic-microscopic model that was used to obtain the potential-energy surfaces [18]. The fragment shapes

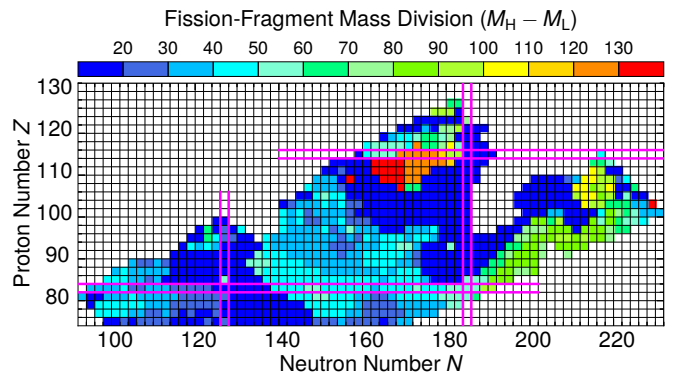


Fig. 2. Calculated heavy and light fission fragment mass differences $M_{\text{H}} - M_{\text{L}}$, following fission of heavy nuclei, analogous to fig. 1 in other respects.

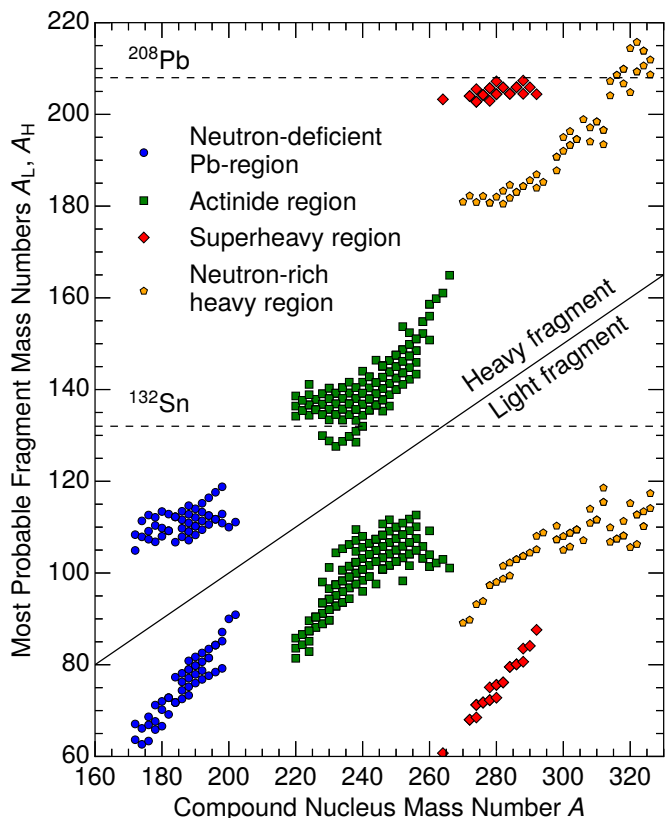


Fig. 3. Calculated most probable fission-fragment mass numbers following fission of neutron-deficient ($74 \leq Z \leq 86$, $92 \leq N \leq 126$), actinide ($74 \leq Z \leq 96$, $132 \leq N \leq 186$), superheavy ($106 \leq Z \leq 114$, $156 \leq N \leq 178$) and neutron-rich ($82 \leq Z \leq 110$, $188 \leq N \leq 218$) nuclides. Only nuclides with asymmetric fission and with a symmetric-yield to peak-yield ratio less than 0.2 are included (red squares in fig. 1).

at scission are taken as the spheroidal shapes characterized by the ε_2 values in the 5D shape parametrization, while the ground-state shapes include $\varepsilon_2, \varepsilon_4, \varepsilon_6$.

The Q^* value is calculated from eq. (2) and E_{TKE} from eq. (4). The TKE value is then obtained from eq. (3). The TKE yield $Y(E_{\text{TKE}})$ is the percentage of fission events per MeV kinetic energy, while the average TKE is the kinetic energy of the relative motion of two fission fragments averaged over all fission events.

3 Calculated results

3.1 Fission-fragment mass distributions

The calculated regions of symmetric and asymmetric fission in the full region of study are shown in fig. 1. The results agree very well with fig. 3 in ref. [6] in which the lower part of the region in fig. 1 is shown. Figure 1 also shows the upper part of the asymmetric-fissioning actinide region as well as an additional region of asymmetry, approximately $108 \leq Z \leq 116$ and $164 \leq N \leq 176$. There

are no experimental studies of the whole region shown in fig. 1 but studies of 70 nuclides from $Z = 85$ to $Z = 94$ were presented in ref. [19]. It was suggested there that the transition between symmetric fission in the lighter actinide region and asymmetric for heavier actinides is $A \approx 226$. It is further stated that this is somewhat surprising since one would expect both protons and neutrons to affect what regions fission symmetrically or asymmetrically. However, in ref. [19] fission mass distributions across the line $A \approx 226$ are obtained for only a few proton numbers, namely $Z = 89, 90$ and 91 . Here, and in ref. [6], which covers a larger, contiguous region of nuclides than the experimental work, the results show that both protons and neutrons affect asymmetry. Particularly interesting is that above $Z \approx 88$ ($N \approx 132$) the calculated transition line is clearly not a constant mass number A , but approximately a constant $N - Z$ for a range of about eight proton numbers. This prediction has yet to be tested experimentally.

The calculated mass difference between the heavy and light fragments is presented in fig. 2. Soon after the discovery of fission it was observed that the mass of the heavy fragment remains relatively constant at $A \approx 140$, as the mass number of the fissioning system evolves from $A \approx 230$ towards heavier systems. Consequently the light mass increases so the heavy/light fragment mass difference decreases as the fissioning system becomes heavier. This is particularly the case towards the neutron-deficient region where experimental data exists. Striking in fig. 2 is the abrupt transition to a small region (around $Z \approx 110$, $N \approx 166$) of very large differences between the heavy and light fragment masses as well as a very low symmetric to asymmetric yield ratio seen in fig. 1.

This is illustrated in a complementary way in fig. 3 where heavy and light fragment mass pairs are plotted as coloured symbols. Figure 3 shows that asymmetric fission of actinides with mass number from $A \approx 220$ to $A \approx 246$ corresponds to divisions into a ^{132}Sn -like heavy fragment and the corresponding partner. Similarly, there

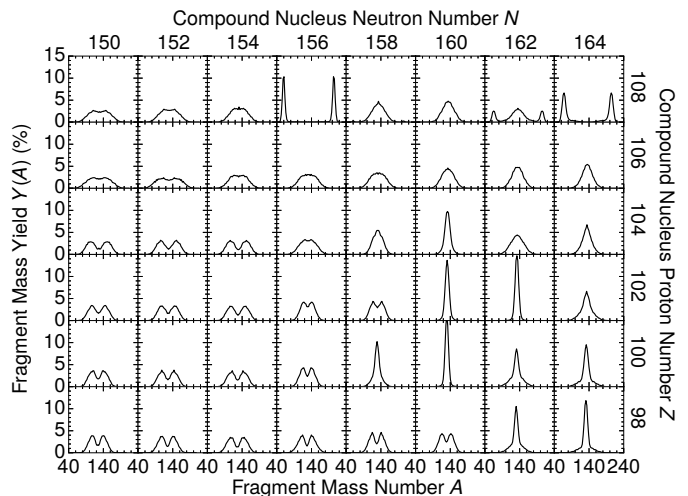


Fig. 4. Calculated fission-fragment mass distributions for fissioning nuclei in the region $98 \leq Z \leq 108$ and $150 \leq N \leq 164$.

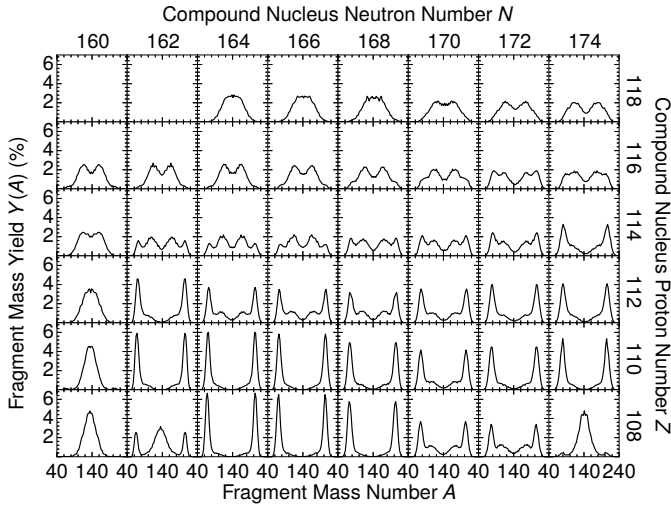


Fig. 5. Calculated fission-fragment mass distributions for fissioning nuclei in the region $108 \leq Z \leq 118$ and $160 \leq N \leq 174$.

is a highly asymmetric region just below and at $Z \approx 114$ corresponding to division into a ^{208}Pb -like heavy fragment and the corresponding partner. In the superheavy region, a ^{208}Pb -like fission fragment is compatible with recent results based on density functional theory [20,21], whereas recent calculations using a prescission point model predicts divisions into a ^{132}Sn -like light fragment and the corresponding partner [22].

It was observed in ref. [23] that the potential-energy surfaces for some superheavy nuclei, for example ^{272}Ds

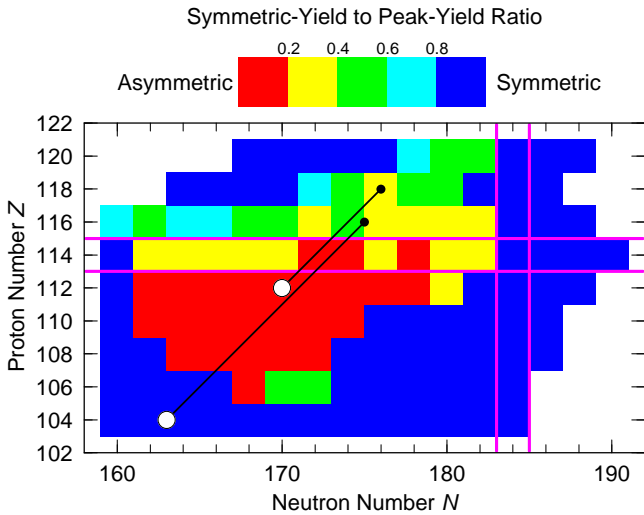


Fig. 6. Calculated symmetric-yield to peak-yield ratios versus N and Z for nuclides in the region of observed superheavy elements, for even-even nuclides. We show some representative observed decay chains with a small solid black dot indicating the start of the decay and the larger solid white dot indicating the termination by spontaneous fission. Pairs of thin parallel lines indicate magic neutron and proton numbers.

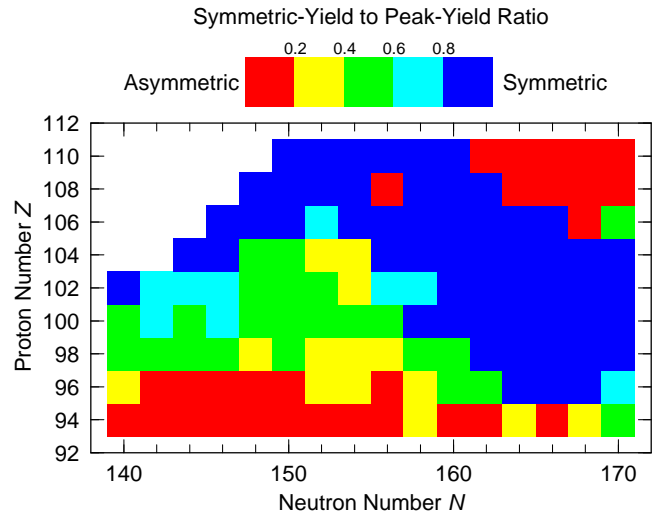


Fig. 7. Calculated symmetric-yield to peak-yield ratios versus N and Z for even-even nuclides in the Fm region.

(see fig. 7 in ref. [23]), exhibit the usual fission valley but also a fusion valley higher in energy than the fission valley and separated from the fission valley by a pronounced ridge. Its existence might be an additional reason that some “cold” fusion reactions have led to evaporation residue creation; the ridge between fusion valley and fission valley hinders the fusion trajectory to deflect into the fission valley before a compound nucleus is created [23]. It might be tempting to predict symmetric fission because the fission valley for this nucleus corresponds to symmetric shapes. On the other hand small neck radii are reached at much lower Q_2 values in the fusion valley than in the fission valley. In this and many other cases it is obviously hard to predict fission mass divisions from our limited ability to understand the details of the calculated multi-dimensional potential-energy surface. However, the BSM method constitutes a well-defined approach to calculate fission mass yields. For many nuclei in this region

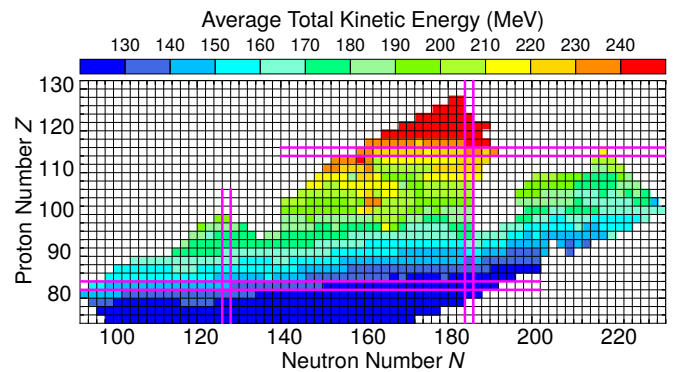


Fig. 8. Calculated average fission-fragment total kinetic energies following fission of heavy nuclei.

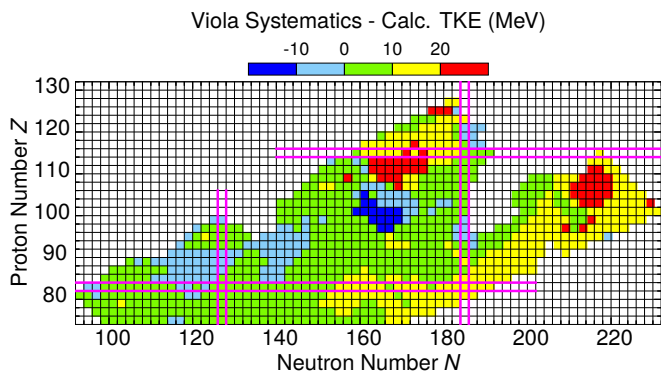


Fig. 9. Viola TKE systematics minus calculated average TKE.

the result is highly asymmetric fission, paradoxically corresponding to fission in the fusion valley.

Some specific, calculated, yield distributions are presented in figs. 4 and 5 in which the highly variable and rapidly changing character of the distributions is readily apparent. The calculated mass yields in fig. 4 show several similarities with the yields obtained using a scission-point model [24,25], though the exact transition points from asymmetric to symmetric fission in this region differ slightly. Nuclides around the superheavy region exhibit modes leading to both symmetric fission and highly asymmetric fission (cf. $(Z, N) = (108, 162)$ in fig. 5). Due to the subtle competition between these two modes, there can be abrupt changes in yields between neighbouring nuclides (e.g. $(Z, N) = (108, 156)$).

There are some observations of fission kinetic energies in the superheavy region, normally in fission events that terminate α -decay chains, but it is hard to draw conclusions about the asymmetry of fission due to the very few

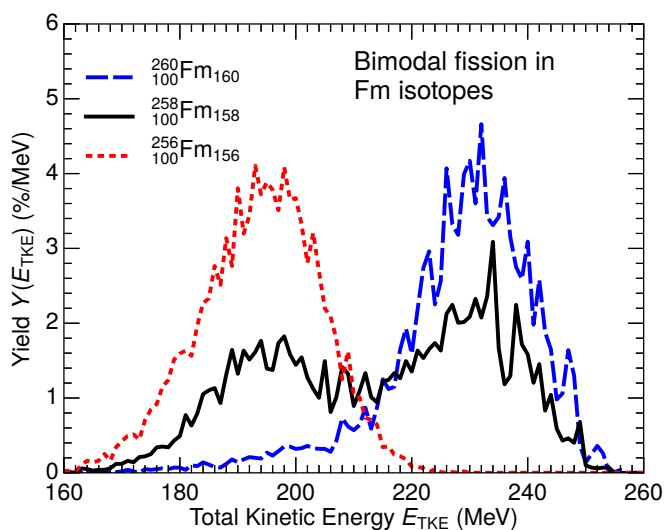


Fig. 10. Calculated fission-fragment total kinetic-energy distributions following low-energy fission of the three nuclides $^{256,258,260}\text{Fm}$.

events observed. Some observations of such fission events are reported in ref. [26]. Sometimes a high TKE value is associated with symmetric fission, in particular for some Fm isotopes where the scission configuration is very compact. However, if the fission configuration is “liquid-drop-like” symmetric fission would correspond to elongated scission shapes and a low TKE. Therefore, a TKE value by itself is not sufficient to establish if fission is symmetric or asymmetric. We show in fig. 6 an enlarged portion of fig. 1 and two examples of decay chains discussed in ref. [26] and their termination by fission at the decay-chain endpoints.

Figure 7 shows an enlarged display of the symmetric-yield to peak-yield ratio in Fig. 1 to enhance details in the vicinity of $^{258}\text{Fm}_{158}$. The transition from asymmetric to symmetric fission at $^{258}\text{Fm}_{158}$ is very visible in this figure as well as in fig. 4. In this region there are also drastic variations of TKE distributions, so we now discuss the results obtained for these distributions.

3.2 Fission-fragment TKE distributions

The calculated average TKE values (see sect. 2.2 for details about the method used) for the entire region of study are shown in fig. 8. Obviously the TKE increases for heavier nuclides and towards the neutron drip line. More easily interpretable is the difference between the Viola TKE systematics [27]

$$E_{\text{TKE}}^{(\text{Viola})} = 0.1189Z^2/A^{1/3} + 7.3 \text{ MeV}, \quad (7)$$

and the actually calculated average TKE. This is illustrated in fig. 9. The substantial abrupt local variations seen in the region near ^{258}Fm are also seen experimentally [28,29,30,31,32]. In their main features, the measurements are well reproduced in the calculations. In the region of very asymmetric fission below $Z = 114$ ($N \approx 162$ – 174) the TKE is lower than the systematics as would be expected. Also in the heavy neutron-rich region ($N \approx 210$ – 220), where we obtain asymmetric fission yields, the average TKE is lower than given by the Viola systematics.

Figure 10 shows in detail the TKE distributions for the three isotopes ^{256}Fm , ^{258}Fm , and ^{260}Fm . The transition from “normal” TKE to high TKE is dramatic, with ^{258}Fm exhibiting a clear “bimodal” structure, as has been seen experimentally [31]. A bimodal structure in the Fm region has also been obtained within the scission-point model [24].

4 Summary

The BSM method [3], which in systematic calculations was previously applied to nuclides from $Z = 74$ to $Z = 94$ [6], has here been used to perform systematic yield calculations in the region $74 \leq Z \leq 126$ and $92 \leq N \leq 230$ for 896 even-even nuclides. Where there is overlap with the previous calculations there is good agreement. Results above $Z = 94$ show for the first time predictions based on the BSM method for the heavier actinide region and the

superheavy region. In the vicinity of $Z = 114$ there is a new, smaller region of asymmetry corresponding to ^{208}Pb -like heavy fragments. Neutron-rich nuclei near the neutron drip line are also predicted to fission asymmetrically.

The authors are grateful to D. Rudolph and C. Schmitt for valuable discussions and suggestions. This work was supported by the Swedish Natural Science Research Council (S.Å.) and the Knut and Alice Wallenberg Foundation (grant No. KAW 2015.0021) (M.A., B.G.C. and S.Å.); J.R. was supported in part by the NNSA DNN R&D of the U.S. Department of Energy and acknowledges a Visiting Professorship at Mathematical physics at Lund University.

References

1. Special Issue on Superheavy Elements (Eds. Ch.E. Düllmann, R.-D. Herzberg, W. Nazarewicz, and Yu.Ts. Oganessian), Nucl. Phys. A **944** (2015).
2. J. Khuyagbaatar, A. Yakushev, Ch.E. Düllmann, D. Ackermann, L.-L. Andersson, M. Block, H. Brand, J. Even, U. Forsberg, W. Hartmann, R.-D. Herzberg, F.P. Heßberger, J. Hoffmann, A. Hübner, E. Jäger, J. Jeppsson, B. Kindler, J.V. Kratz, J. Krier, N. Kurz, B. Lommel, M. Maiti, S. Minami, D. Rudolph, J. Runke, L.G. Sarmiento, M. Schädel, B. Schausten, J. Steiner, T. Torres De Heidenreich, J. Uusitalo, N. Wiehl, and V. Yakusheva, EPJ Web of Conferences **131**, 03003 (2016).
3. J. Randrup and P. Möller, Phys. Rev. Lett. **106**, 132503 (2011).
4. J. Randrup and P. Möller, Phys. Rev. C **88**, 064606 (2013).
5. A.N. Andreyev M. Huyse, and P. Van Duppen, Rev. Mod. Phys. **85**, 1541 (2013).
6. P. Möller and J. Randrup, Phys. Rev. C **91**, 044316 (2015).
7. J. Randrup, P. Möller, and A.J. Sierk, Phys. Rev. C **84**, 034613 (2011).
8. P. Möller, J. Randrup, and A.J. Sierk, Phys. Rev. C **85**, 024306 (2012).
9. D.E. Ward, B.G. Carlsson, T. Døssing, P. Möller, J. Randrup, and S. Åberg, Phys. Rev. C **95**, 024618 (2017).
10. P. Möller, A.J. Sierk, T. Ichikawa, A. Iwamoto, R. Bengtsson, H. Uhrenholt, and S. Åberg, Phys. Rev. C **79**, 064304 (2009).
11. P. Möller, J.R. Nix and W.J. Swiatecki, Proc. 50 Years with Nuclear Fission, Gaithersburg, 1989 (American Nuclear Society, La Grange Park, 1989) p. 153.
12. P. Möller and J.R. Nix, J. Phys. G **20**, 1681 (1994).
13. S.G. Nilsson, C.F. Tsang, A. Sobiczewski, Z. Szymański, S. Wycech, C. Gustafson, I.-L. Lamm, P. Möller, and B. Nilsson, Nucl. Phys. A **131**, 1 (1969).
14. M. Bolsterli, E.O. Fiset, J.R. Nix, and J.L. Norton, Phys. Rev. C **5**, 1050 (1972).
15. P. Möller, J.R. Nix, and W.J. Swiatecki, Nucl. Phys. A **492**, 349 (1989).
16. P. Möller, D.G. Madland, A.J. Sierk, and A. Iwamoto, Nature **409**, 785 (2001).
17. M. Albertsson, B.G. Carlsson, T. Døssing, P. Möller, J. Randrup, and S. Åberg, submitted for publication, arXiv:1811.02283.
18. P. Möller, A.J. Sierk, and A. Iwamoto, Phys. Rev. Lett. **92**, 072501 (2004).
19. K.-H. Schmidt, S. Steinhäuser, C. Böckstiegel, A. Grewe, A. Heinz, A.R. Junghans, J. Benlliure, H.-G. Clerc, M. de Jong, J. Müller, M. Pfützner, and B. Voss, Nucl. Phys. A **665**, 221 (2000).
20. M. Warda, A. Zdeb and L.M. Robledo, Phys. Rev. C **98**, 041602(R) (2018).
21. Z. Matheson, S.A. Giuliani, W. Nazarewicz, J. Sadhukhan, and N. Schunck, Phys. Rev. C **99**, 041304 (2019).
22. N. Carjan, F.A. Ivanyuk, and Yu.Ts. Oganessian, Phys. Rev. C **99**, 064606 (2019).
23. T. Ichikawa, A. Iwamoto, P. Möller, and A.J. Sierk, Phys. Rev. C **71**, 044608 (2005).
24. N. Carjan, F.A. Ivanyuk, Yu. Oganessian, G. Ter-Akopian, Nucl. Phys. A **942**, 97 (2015).
25. H. Paşca, A.V. Andreev, G.G. Adamian, and N.V. Antonenko, Phys. Rev. C **97**, 034621 (2018).
26. Yu.Ts. Oganessian, J. Phys. G: Nucl. Part. Phys. **34**, R165 (2007).
27. V.E. Viola, K. Kwiatkowski, and M. Walker, Phys. Rev. C **31**, 1550 (1985).
28. W. John, E.K. Hulet, R.W. Lougheed, and J.J. Wesolowski, Phys. Rev. Lett. **27**, 45 (1971).
29. D.C. Hoffman, J.B. Wilhelmy, J. Weber, W.R. Daniels, E.K. Hulet, R.W. Lougheed, J.H. Landrum, J.F. Wild, and R.J. Dupzyk, Phys. Rev. C **21**, 972 (1980).
30. E.K. Hulet, R.W. Lougheed, J.H. Landrum, J.F. Wild, D.C. Hoffman, J. Weber, and J.B. Wilhelmy, Phys. Rev. C **21**, 966 (1980).
31. E.K. Hulet, J.F. Wild, R.J. Dougan, R.W. Lougheed, J.H. Landrum, A.D. Dougan, M. Schädel, R.L. Hahn, P.A. Baisden, C.M. Henderson, R.J. Dupzyk, K. Sümmerner, and G.R. Bethune, Phys. Rev. Lett. **56**, 313 (1986).
32. E.K. Hulet, J.F. Wild, J. Dougan, R.W. Lougheed, J.H. Landrum, A.D. Dougan, P.A. Baisden, C.M. Henderson, R.J. Dupzyk, R.L. Hahn, M. Schädel, K. Sümmerner, G.R. Bethune, Phys. Rev. C **40**, 770 (1989).